Evidence of Langmuir/ Z -mode Wave Decay into Z -mode Electromagnetic Radiation in the Solar Wind

F J Polanco-Rodríguez, C. Krafft, P. Savoini

▶ **To cite this version:**

F J Polanco-Rodríguez, C. Krafft, P. Savoini. Evidence of Langmuir/ Z -mode Wave Decay into Z -mode Electromagnetic Radiation in the Solar Wind. The Astrophysical Journal Letters, 2026, 1002 (2), pp.L35. ⟨10.3847/2041-8213/ae626f⟩. ⟨hal-05615478⟩

HAL Id: hal-05615478

https://hal.science/hal-05615478v1

Submitted on 7 May 2026

HAL is a multi-disciplinary open access archive for the deposit and dissemination of scientific research documents, whether they are published or not. The documents may come from teaching and research institutions in France or abroad, or from public or private research centers.

L'archive ouverte pluridisciplinaire **HAL**, est destinée au dépôt et à la diffusion de documents scientifiques de niveau recherche, publiés ou non, émanant des établissements d'enseignement et de recherche français ou étrangers, des laboratoires publics ou privés.

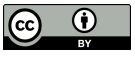

Distributed under a Creative Commons CC BY 4.0 - Attribution - International License

The Astrophysical Journal Letters, 1002:L35 (9pp), 2026 May 10 https://doi.org/10.3847/2041-8213/ae626f
© 2026. The Author(s). Published by the American Astronomical Society.
OPEN ACCESS

Evidence of Langmuir/$\mathcal{Z}$-mode Wave Decay into $\mathcal{Z}$-mode Electromagnetic Radiation in the Solar Wind

F. J. Polanco-Rodríguez[1], C. Krafft[1,2], and P. Savoini[1]
[1] Laboratoire de Physique des Plasmas (LPP), CNRS, Sorbonne Université, Observatoire de Paris, Université Paris-Saclay, Ecole polytechnique, Institut Polytechnique de Paris, 91120 Palaiseau, France; catherine.krafft@universite-paris-saclay.fr
[2] Institut Universitaire de France (IUF), Paris, France
Received 2026 February 10; revised 2026 April 20; accepted 2026 April 21; published 2026 May 6

Abstract

The nonlinear decay of Langmuir/$\mathcal{Z}$-mode waves into electromagnetic $\mathcal{Z}$-mode wave radiation near the plasma frequency is observed for the first time in the solar wind, during the encounter of the Solar Orbiter satellite with an electron beam associated with a type III radio burst. This result was achieved through the high-resolution electric and magnetic field measurements provided by the Radio Plasma Waves instrument on board the spacecraft. The decay process is identified through multiple lines of evidence: satisfaction of Doppler-shifted frequency resonance conditions, strong phase coherence and temporal coincidence between the interacting waves, dominance over competing mechanisms, and full agreement with theoretical predictions. Two-dimensional particle-in-cell simulations, conducted under close beam-plasma conditions, successfully reproduce the key features of the observations. Notably, they suggest that the wave packet observed by Solar Orbiter may be trapped within an extended, nearly flat-bottomed density well, where the decay process is not overcome by wave scattering on random density fluctuations and subsequent mode conversion effects.

Unified Astronomy Thesaurus concepts: Solar wind (1534); Radio bursts (1339); Space plasmas (1544); Solar flares (1496); Solar radio emission (1522)

1. Introduction

Despite decades of routine observations of type III solar radio bursts in the solar wind, key questions regarding their radio emission mechanisms remain unanswered. With the advent of recent missions such as Solar Orbiter (D. Müller et al. 2020) and Parker Solar Probe (N. J. Fox et al. 2016), long-duration and well-resolved electric and magnetic waveforms are now recorded (S. D. Bale et al. 2016; M. Maksimovic et al. 2020). More specifically, recent advances in magnetometry have enabled the analysis of highly resolved magnetic waveforms (G. Jannet et al. 2021). Such measurements should help evidence and untangle the wave processes that lead to electromagnetic waves radiated at the plasma frequency f_p and its harmonic $2f_p$ during radio bursts (e.g., I. C. Jebaraj et al. 2023; M. Kretzschmar et al. 2026; B. Ma et al. 2026).

Although Langmuir/$\mathcal{Z}$-mode waves (hereafter referred to as $\mathcal{LZ}$ waves) have been observed and studied in the solar wind using satellites such as Stereo and Wind (e.g., S. D. Bale et al. 1998, 2000; P. Henri et al. 2009; D. M. Malaspina et al. 2011; D. B. Graham & I. H. Cairns 2013; P. J. Kellogg et al. 2013), evidence for and detailed analyses of their magnetic signatures in the solar wind have emerged only recently. In this context, A. Larosa et al. (2022) used data from Parker Solar Probe to provide the first unambiguous observation of the magnetic component of a $\mathcal{Z}$-mode wave in the solar wind, which corresponds to the slow extraordinary electromagnetic mode with frequency below the local plasma frequency (e.g., D. Krauss-Varban 1989). The authors proposed the scattering of $\mathcal{LZ}$ waves on density fluctuations as the primary mechanism that generates such waves. More recently, T. Formánek et al. (2025) examined a high-amplitude wave packet observed by Solar Orbiter on 2022 September 22 at 13:52:28 UT. By analyzing electron beam velocity distribution functions (VDFs) at two distinct times and applying linear wave theory, they reported obliquely propagating $\mathcal{LZ}$ waves and estimated their polarization as well as their wavevector, characterized by a magnitude $k\lambda_D \sim 10^{-3}$ (λ_D is the Debye length) and a propagation angle θ between $\boldsymbol{k}$ and the ambient magnetic field. This value of k is smaller than that expected for beam-driven waves, and corresponds to a frequency of $f \lesssim f_p$ consistent with a $\mathcal{Z}$-mode wave.

Theoretical and numerical studies have shown that, even though linear mode conversion (LMC) at constant frequency of beam-generated $\mathcal{LZ}$ wave turbulence proves more efficient for generating $\mathcal{Z}$-mode waves in weakly magnetized plasmas with nonnegligible density turbulence (C. Krafft & A. S. Volokitin 2025; C. Krafft et al. 2025; F. Polanco-Rodríguez et al. 2025a), nonlinear decay of $\mathcal{LZ}$ waves serves as an effective mechanism in nearly homogeneous solar wind regions (C. Krafft et al. 2024b; F. Polanco-Rodríguez et al. 2025b, 2026). This work aims to show that this decay process is responsible for the $\mathcal{Z}$-mode waves observed by Solar Orbiter on 2022 September 22 at 13:52:28 UT.

Through a detailed analysis of the corresponding data, we present the first observational evidence in the solar wind of the nonlinear three-wave decay of $\mathcal{LZ}$ waves into electromagnetic $\mathcal{Z}$-mode radiation at f_p. Our findings are supported by multiple lines of evidence: waveform analysis revealing high cross-bicoherence levels, fulfillment of Doppler-shifted frequency resonance conditions—involving frequencies and wavevectors in the solar wind frame—assessment of the decay threshold and turbulence parameter, examination of low-frequency wave dynamics, dominance over alternative generation mechanisms,

Original content from this work may be used under the terms of the Creative Commons Attribution 4.0 licence. Any further distribution of this work must maintain attribution to the author(s) and the title of the work, journal citation and DOI.

and consistency with our earlier theoretical predictions (F. Polanco-Rodríguez et al. 2025b, 2026).

In addition, we present a second event detected by Solar Orbiter, which further confirms the same nonlinear mechanism at work. Our analysis integrates magnetic waveform observations with wave phase coherence analysis, two-dimensional theoretical modeling, and direct comparison to particle-in-cell (PIC) simulations, which replicate the observed decay processes. Together, these elements provide, compared to previous analyses of $\mathcal{LZ}$ wave decay, an unprecedented level of evidence that robustly identifies the underlying physical mechanism.

Furthermore, the direct comparison of waveforms recorded in simulations and by Solar Orbiter enriches the discussion and provides deeper insights. It offers strong support for the wave generation mechanism while suggesting some key properties of the density turbulence in the plasma region where the waves are observed, thereby clarifying its role in the wave dynamics. Finally, while LMC at constant frequency is typically more efficient than wave decay for $\mathcal{Z}$-mode radiation at f_p, the latter can become dominant when wave packets reach very large amplitudes in extended density wells where they are trapped. The Solar Orbiter observations presented here align with this scenario.

2. Instruments and Data Acquisition

The data analyzed below have been recorded by the Time Domain Sampler (TDS) of the Radio and Plasma Waves (RPW) instrument on board Solar Orbiter (M. Maksimovic et al. 2020). The TDS (J. Soucek et al. 2021) provides survey mode measurements of electric and magnetic field components, with a sampling rate of 262 kHz, offering highly resolved waveforms with typical durations of 62 ms. The recorded data consist of two electric field components E_y and E_z—obtained through the measurements of three voltages between coplanar antennas—in the Satellite Reference Frame (SRF), and of a magnetic field component B measured along the x-axis of the Search Coil Magnetometer's frame. During normal operation, the TDS captures a waveform snapshot every second. The onboard software then analyzes each of them, classifies them into distinct categories, and determines if they are valuable enough to be transferred to Earth.

The two snapshots analyzed below, chosen as representative examples from a broader set of observations, were captured on 2022 September 22 at 13:52:28 UT and 14:05:04 UT. A type III solar radio burst was observed during the spacecraft's encounter with a relativistic electron beam (T. Formánek et al. 2025). In the SRF, the solar wind speed measured at 13:52:28 UT by the Solar Wind Analyzer is $\boldsymbol{V}_{\rm sw} \simeq (-325.1, -11, 5)\,{\rm km\,s^{-1}}$, while the onboard Magnetometer provides the ambient magnetic field $\boldsymbol{B}_0 = (-9.4, 11.6, 5)$ nT. Later, at 14:05:04 UT, these values have slightly changed, as $\boldsymbol{V}_{\rm sw} \simeq (-326, -2, 0)\,{\rm km\,s^{-1}}$ and $\boldsymbol{B}_0 = (-8.7, 9.5, 7.4)$ nT. Measurements of the plasma frequency were done by the Thermal Noise Analyzer at 13:52 and 14:14 UT, providing $f_p \simeq 47.2$ kHz and $f_p \simeq 58.5$ kHz, respectively. Then, the magnetization ratio can be estimated as $f_c/f_p \simeq 0.01$ for both events. On the other hand, the beam energy and the plasma electron temperature measured at 13:38 UT are $\mathcal{E}_b \simeq 23.9$ keV and $T_e \simeq 11.7$ eV (T. Formánek et al. 2025), leading to $v_b \simeq 0.21c \simeq 43.7 v_T$ and $v_T \simeq 0.0048c$. A second measurement is available at 14:05 UT, when the electron beam is decelerated, providing $T_e = 11.9$ eV.

3. Evidence of Nonlinear Wave Decay Leading to $\mathcal{Z}$-mode Waves

3.1. Description of the Event at 13:52:28 UT

Figure 1 presents the event recorded by Solar Orbiter on 2022 September 22 at 13:52:28 UT, during the detection of a type III burst-related electron beam. The waveforms of the electric field components $E_y(t)$ and $E_z(t)$ are shown in Figure 1(a). A large-amplitude wave packet reaching 150 mV m^{-1} is observed around $t \simeq 10$ ms. At the same time, the hodograms in panel (b) clearly demonstrate elliptic polarization, excluding purely electrostatic waves. Meanwhile, the high-frequency electric energy spectrogram shows wave packets excited around $f \simeq 45.8$ kHz. At the same time, the low-frequency spectrogram exhibits waves mainly excited near $f \sim 0.3$ kHz, below the ion plasma frequency $f_{pi} \simeq 1$ kHz (Figure 1(d)). Finally, the high-frequency magnetic energy spectrogram (Figure 1(e)) shows a distinct emission at the same time and frequencies as the electric energy, which is consistent with the expected behavior of electromagnetic $\mathcal{Z}$-mode waves.

Figure 1(f) displays the power spectra of the fields E_z, E_y, and B across a wide frequency range, all showing strong excitation near 46 kHz. Zoomed-in views in Figures 1(g) and (h) provide precise measurements of the most intense spectral peaks at $f_1 \simeq 46.04$, $f_2 \simeq 45.87$, and $f_3 \simeq 45.74$ kHz, excited with the energy ratio $(E/cB)^2 \sim 10^4$ (E is the total electric field amplitude). The magnetic energy spectrum mirrors these peaks, while the low-frequency electric energy spectrum features a broad, prominent peak at $f_1' \simeq 0.3$ kHz—without a magnetic counterpart above the noise level.

The high-frequency peaks fall within the expected range for beam-generated $\mathcal{LZ}$ waves. Indeed, the $\mathcal{LZ}$ wave Doppler-shifted frequencies are given by $f_{\mathcal{LZ}} = f^{\rm sw}_{\mathcal{LZ}}(\boldsymbol{k}) + \boldsymbol{k}\cdot\boldsymbol{V}_{\rm sw} \simeq f_p(1 + 3k^2\lambda_D^2/2 + (V_{\rm sw}/v_T)k\lambda_D\cos\theta_{\rm sw})$, where $f^{\rm sw}_{\mathcal{LZ}}(\boldsymbol{k})$ are the frequencies in the solar wind frame; $\theta_{\rm sw}$ is the angle between the $\mathcal{LZ}$ wavevector $\boldsymbol{k}$ and the solar wind velocity $\boldsymbol{V}_{\rm sw}$ ($|\boldsymbol{V}_{\rm sw}| = V_{\rm sw} \simeq 330\,{\rm km\,s^{-1}} \simeq 0.23\,v_T$). Note that the magnetic corrections to this dispersion are second order in f_c and thus negligible here, given that $f_c/f_p \simeq 0.01$. The frequency range of beam-driven $\mathcal{LZ}$ waves can then be estimated for any θ as $45.6 \leqslant f_{\mathcal{LZ}} \leqslant 46.06$ kHz, which aligns closely with the frequency band in which the large-amplitude wave packet is observed (Figures 1(f)–(h)). We have considered that $k\lambda_D \simeq k_b\lambda_D \simeq v_T/v_b \simeq 0.023$, where k_b is the characteristic wavenumber of beam-driven $\mathcal{LZ}$ waves, and have defined the plasma frequency as $f_p \simeq f_3 \simeq 45.74$ kHz, as explained below.

3.2. Evidence for $\mathcal{LZ}$ Wave Decay

We show in the following that the emissions observed in Figure 1, which were identified by T. Formánek et al. (2025) as oblique propagating $\mathcal{LZ}$ waves with small wavenumbers $k\lambda_D \sim 10^{-3}$, can arise from nonlinear wave decay, as supported by the arguments presented below :

1. Doppler-shifted frequency resonance conditions between three time-synchronized waves are fulfilled.
2. The observed high- and low-frequency wave dynamics align with theoretical predictions of $\mathcal{LZ}$ wave decay in weakly magnetized plasmas.

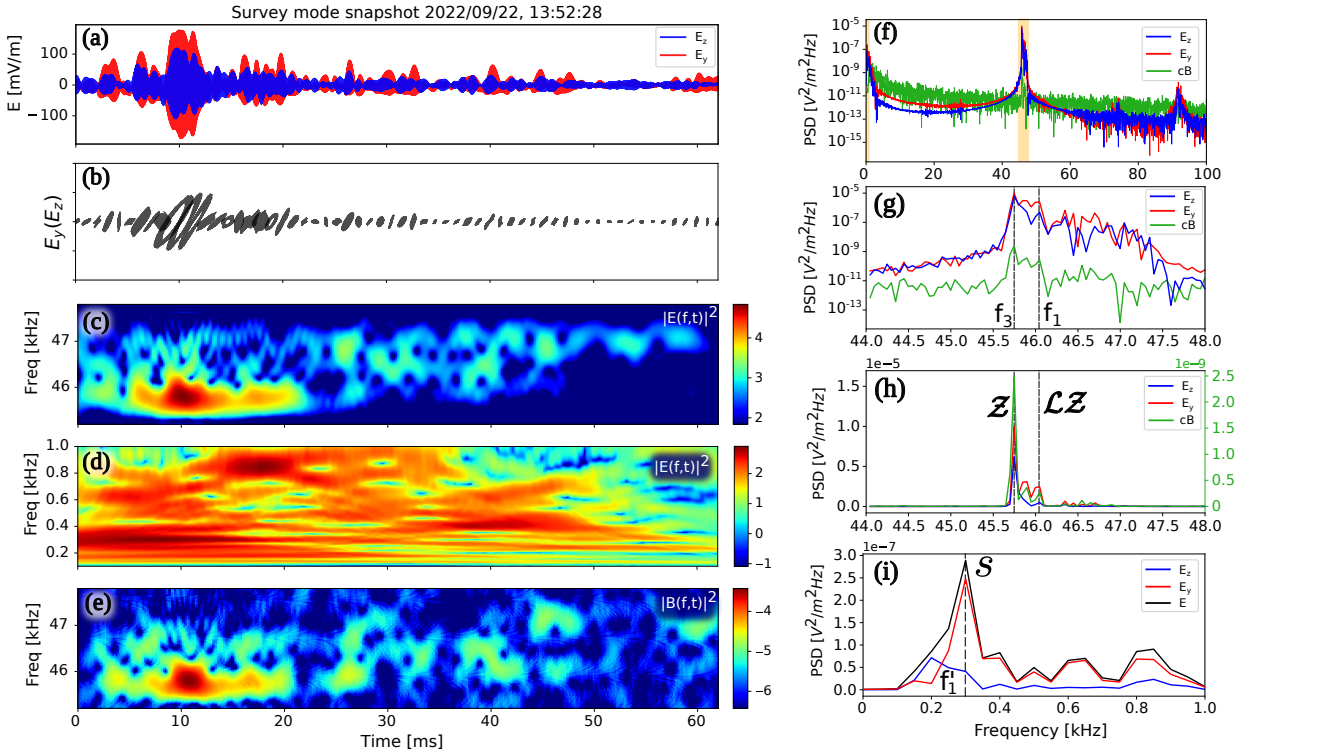

Figure 1. Snapshot captured in the survey mode by the Solar Orbiter instrument RPW, on 2022 September 22, at 13:52:28 UT. (a) Waveform of the two electric field components E_z (blue) and E_y (red), in the SRF frame. (b) Hodograms $E_y(E_z)$ calculated within equidistant time windows of 0.7 ms. (c)–(d) Wavelet spectrograms of the electric energy $|E(f,t)|^2 = |E_y(f,t)|^2 + |E_z(f,t)|^2$ in the high- and low-frequency ranges, i.e., $45 \leqslant f \leqslant 48$ kHz and $f \leqslant 1$ kHz, respectively. (e) Wavelet spectrogram of the magnetic energy $|B(f,t)|^2$, in the same frequency range as (c). (c)–(e) The color bars are in logarithmic scales. (f)–(i) Power spectra of the field components E_z (blue), E_y (red), and cB (green), respectively. Zoomed-in views are presented, in logarithmic and linear scales, in the ranges of $44 \leqslant f \leqslant 48$ kHz ((g), (h)) and $f \leqslant 1$ kHz (i). The black curve in (i) represents the spectrum of $|E|^2$. The dashed vertical lines correspond to peaks at $f_3 \simeq 45.74$ kHz and $f_1 \simeq 46.04$ kHz (g)–(h), and at $f_1' \simeq 0.3$ kHz (i). Spectra in (f)–(i) are calculated in the time interval of $2 \leqslant t \leqslant 22$ ms.

3. Quantitative estimates of the wave turbulence parameter and the decay threshold support the occurrence of this process.
4. The process is dominant over alternative mechanisms.
5. Cross-bicoherence diagnostics confirm strong phase coherence between the interacting waves.

Further sections provide additional conclusive evidence, including the observation of a second event with similar characteristics and wave decay, along with 2D/3V PIC simulations that remarkably reproduce the observed waveforms and validate the underlying mechanism.

3.2.1. Three-wave Resonance Conditions

The waves emitted at frequencies f_1, f_3, and f_1' in Figures 1(g)–(i) satisfy the resonance condition $f_1 \simeq f_3 + f_1'$ with very good accuracy, as $f_1 \simeq 46.04$ kHz and $f_3 + f_1' \simeq (45.74 + 0.3)$ kHz $= 46.04$ kHz. Because this relationship connects Doppler-shifted frequencies, it also infers the same conditions for wavevectors in the solar wind frame. Furthermore, spectrograms indicate that the three corresponding wave packets appear simultaneously around $t \sim 10$ ms (Figures 1(c)–(e)). These findings suggest that the wave emitted at the lowest frequency $f_{\mathcal{Z}} = f_3$, which carries the highest magnetic energy, may correspond to a $\mathcal{Z}$-mode wave generated by decay of a mother $\mathcal{LZ}$ wave excited at $f_{\mathcal{LZ}} = f_1$, together with low-frequency waves appearing at $f_{\mathcal{S}} = f_1'$, through the channel $\mathcal{LZ} \longrightarrow \mathcal{Z} + \mathcal{S}$. If this hypothesis holds—and further evidence supports it—then the dispersive properties of $\mathcal{Z}$-mode waves and the kinematics of the decay imply that these waves must be produced just below f_p and very close to it (F. Polanco-Rodríguez et al. 2025b). Based on this assumption, the plasma frequency at the exact moment of waveform capture can be estimated as $f_p \simeq 45.74$ kHz. This estimate is used exclusively in Section 3.1 to determine the frequency range in which waves are excited and is not necessary to demonstrate decay.

Based on theoretical studies (e.g., K. Akimoto 1989; F. Polanco-Rodríguez et al. 2025b) and previous PIC simulations conducted with close parameters (C. Krafft & P. Savoini 2024a), the absence of a magnetic signature at low frequencies and the very weak plasma magnetization measured ($f_c/f_p = 0.01$), the observed low-frequency waves are expected to correspond to ion acoustic waves. Moreover, according to the measured electron-to-ion temperature ratio $T_e/T_i \sim 3$, such waves are expected to be significantly damped after approximately 120 ms (S. P. Gary 1993). This timescale is about twice the waveform duration and much longer than the characteristic decay time (∼15 ms), given the large electric field amplitudes (R. Z. Sagdeev & A. A. Galeev 1969). These estimates provide additional support for the occurrence of the decay process.

The intensity of the $\mathcal{LZ}$ mother waves is observed to be approximately five times lower than that of the daughter $\mathcal{Z}$-mode waves (Figure 1(h)). This difference can be explained by two mechanisms that may occur simultaneously. First, the decay results in the transfer of energy from $\mathcal{LZ}$ waves to both the $\mathcal{Z}$-mode and $\mathcal{S}$ waves. Second, in a randomly inhomogeneous plasma, such as the solar wind, a tail of accelerated

beam electrons is formed as a result of $\mathcal{LZ}$ wave scattering on density fluctuations δn, even when their average level $\Delta N = \langle(\delta n/n_0)^2\rangle^{1/2}$ is quite small; these electrons can reabsorb the energy of $\mathcal{LZ}$ waves (C. Krafft et al. 2013, 2023). This suprathermal tail is visible in the VDF measured by Solar Orbiter during the event (see Figure 2 in T. Formánek et al. 2025). Note also that daughter waves have been observed with higher intensity than their mother wave (e.g., P. J. Kellogg et al. 2013).

3.2.2. Dynamics of $\mathcal{LZ}$ Wave Decay in a Weakly Magnetized Plasma

The three wave packets observed at frequencies f_1, f_3, and f_1' are consistent with a single-step $\mathcal{LZ}$ wave decay cascade. Indeed, the wavenumber shift between the mother and daughter high-frequency waves can be approximated by $k_0\lambda_D = 2c_s/3v_T$, where c_s is the ion acoustic velocity (e.g., A. Layden et al. 2013; C. Krafft & P. Savoini 2024a). For the measured value $T_e/T_i \sim 3$, we get $k_0\lambda_D \sim 0.02$. Since $k_0/k_b \simeq 1$ (k_b is the characteristic wavenumber of the beam-driven $\mathcal{LZ}$ waves), only a single decay cascade is expected. Then, the mother $\mathcal{LZ}$ waves transfer their energy directly to $\mathcal{Z}$-mode waves, without redistributing it among other $\mathcal{LZ}$ waves. However, while these estimates are approximate, they do not exclude the possibility of two decay cascades. Observations indicate that $\mathcal{Z}$-mode waves are a terminal decay product. If they were not, their high amplitude would lead to a further decay—a process that is not observed here.

In the one-dimensional approximation, decay cascades of $\mathcal{LZ}$ waves terminate at $k\lambda_D \simeq k_*\lambda_D = (v_T/c)(1 + f_p/f_c)^{-1/2}$ (I. H. Cairns & A. Layden 2018), i.e., at $k\lambda_D \simeq 4.7 \cdot 10^{-4}$ for the plasma conditions of the observed event. In two-dimensional geometry, PIC simulations reveal the formation of a boundary curve $k_*(\theta)$ around $k \sim 0$, on which the energy of decaying waves is ultimately deposited. It can be determined by calculating the isocontour $f_{\mathcal{Z}}(k_\parallel, k_\perp) = f_0$ of the $\mathcal{Z}$-mode wave dispersion relation, where f_0 is the frequency at which the group velocity of $\mathcal{Z}$-mode waves increases sharply, marking the termination of the decay process (F. Polanco-Rodríguez et al. 2025b). Applying the plasma parameters of the observed event, we find $4.7 \cdot 10^{-4} \lesssim k_*(\theta)\lambda_D \lesssim 1.02 \cdot 10^{-3}$ for any θ. On the other hand, by combining electron beam measurements with a linear wave dispersion analysis, T. Formánek et al. (2025) identified the emission at $f \simeq 45.74$ kHz as an oblique $\mathcal{LZ}$ wave with small wavenumber $k\lambda_D \simeq 10^{-3}$ and frequency slightly below f_p, which is in fact a $\mathcal{Z}$-mode wave. This result aligns closely with our theoretical predictions. Rather than coincidental, this consistency provides additional evidence supporting the decay mechanism while helping to rule out weaker alternative mechanisms (Section 3.2.4).

Finally, for the decay process to proceed, the group velocities of the $\mathcal{S}$ and $\mathcal{LZ}$ wave packets must be of a similar order of magnitude. For $T_e/T_i \sim$, we find $c_s/v_T = ((m_e/m_i)(1 + 3T_i/T_e))^{1/2} \simeq 0.033$, while $v_g^{\mathcal{LZ}}/v_T \simeq 3k_b\lambda_D \simeq 0.069$, which, taking into account uncertainties, allows energy exchange between the waves during their propagation.

3.2.3. $\mathcal{LZ}$ Wave Turbulence Intensity

We provide below two additional arguments showing the consistency of our interpretation with nonlinear decay. The observed wave packet displays an exceptionally high intensity, likely driven by the simultaneously detected nonrelaxed electron beam. Despite its large amplitude, there is no indication of strong turbulence phenomena. The turbulence parameter of the $\mathcal{LZ}$ waves can be calculated as $W_{\mathcal{LZ}} = \varepsilon_0|E|^2_{\mathcal{LZ}}/4n_0k_BT_e \simeq 3.5 \cdot 10^{-4}$, where $|E|_{\mathcal{LZ}} \simeq 86$ mV m^{-1} is the peak electric field amplitude of the $\mathcal{LZ}$ waves estimated from the electric field waveform filtered near f_p. In the parameter space ($k\lambda_D$, W), as defined by Zakharov's classification (V. E. Zakharov et al. 1985; P. A. Robinson 1997), the point ($k_b\lambda_D$, $W_{\mathcal{LZ}}$) lies within Region I, where wave decay instability dominates—excluding other processes such as modulational instabilities.

Moreover, for the decay process $\mathcal{LZ} \longrightarrow \mathcal{Z} + \mathcal{S}$ to proceed, the energy carried by the $\mathcal{LZ}$ waves must exceed a specific threshold. This condition can be expressed as $\varepsilon_0|E|^2_{\mathcal{LZ}}/n_0k_BT_e > 4|\gamma_{\mathcal{S}}\gamma_{\mathcal{Z}}|/(f_{\mathcal{S}}f_{\mathcal{Z}})$ (e.g., P. K. Shukla et al. 1983), where $f_{\mathcal{S}}$ and $f_{\mathcal{Z}}$ denote the frequencies of the waves $\mathcal{S}$ and $\mathcal{Z}$, and $\gamma_{\mathcal{S}}$ and $\gamma_{\mathcal{Z}}$ represent their damping rates, respectively. Calculations indicate that the required electric field threshold—on the order of a few millivolts per meter (R. P. Lin et al. 1986; D. B. Graham & I. H. Cairns 2013)—is significantly exceeded.

3.2.4. Dominance over Alternative Mechanisms

Two other mechanisms might appear a priori capable of explaining the observed electromagnetic emission at f_p. The first is the LMC process at constant frequency, which can generate large-amplitude electromagnetic waves in randomly inhomogeneous plasmas (C. Krafft & P. Savoini 2022; C. Krafft et al. 2025; C. Krafft & A. S. Volokitin 2025). However, multiple considerations indicate that LMC is not the dominant mechanism at play here, even if its participation cannot be completely ruled out. First, this mechanism would fail to reproduce the sharp $\mathcal{Z}$-mode peak observed near f_p (Figure 1(h)). Instead, scattering on density fluctuations would result in a broader, smoother peak extending toward lower frequencies down to the $\mathcal{Z}$-mode cutoff frequency. Second, since $f_c/f_p \ll 1$, LMC would generate $\mathcal{X}$-mode waves with energy comparable to that of $\mathcal{Z}$-mode waves (C. Krafft et al. 2025), as well as $\mathcal{O}$-mode waves, which are not observed. Third, if LMC were the primary mechanism, the bicoherence diagnostics and the resonance conditions would lack the clarity and precision found below in Section 3.3, due to their random modifications through wave scattering on density fluctuations.

Another mechanism to consider is electromagnetic decay, where $\mathcal{LZ}$ waves generate $\mathcal{O}$-mode and ion acoustic $\mathcal{S}$ waves through the channel $\mathcal{LZ} \longrightarrow \mathcal{O} + \mathcal{S}$. Although this process could excite low-frequency waves within the recorded frequency ranges, PIC simulations—using parameters closely matching the observations—indicate that the ratio $(E/cB)^2$ reaches $\sim 10^4$ for $\mathcal{Z}$-mode waves (in agreement with observations, see Section 3.1), whereas for $\mathcal{O}$-mode waves, it is at least an order of magnitude lower. This aligns very well with the results of T. Formánek et al. (2025), who report by other means that $(E/cB)^2 \simeq 10^4$ for the observed peak. Consequently, the energy peak at $f_3 = 45.74$ kHz is better explained by nonlinear decay to $\mathcal{Z}$-mode waves than by the two above-mentioned alternative mechanisms.

Finally, other nonlinear wave–wave interactions involving low-frequency modes–beyond ion acoustic waves—can be ruled out. First, no significant magnetic energy is observed at the corresponding frequencies. Second, in weakly magnetized

plasmas such as those studied here ($f_c/f_p \ll 1$), PIC simulations have shown that the low-frequency waves driven by the beam-generated $\mathcal{LZ}$ wave turbulence are primarily ion acoustic modes (F. Polanco-Rodríguez et al. 2025b).

3.3. Cross-bicoherence Diagnostics

To confirm the occurrence of three-wave nonlinear decay, let us look for phase coherence between interacting waves and thus calculate the cross-bicoherence level b_c defined in the frequency plane (f_1, f_2) as

$$b_c(f_1, f_2) = \frac{|\langle X^n(f_1) Y^n(f_2) Z^{n*}(f_1 + f_2)\rangle_n|}{\sqrt{\langle |X^n(f_1)|^2 |Y^n(f_2)|^2\rangle_n \langle |Z^n(f_1 + f_2)|^2\rangle_n}}, \quad (1)$$

where $X(t)$, $Y(t)$, and $Z(t)$ are three wave fields; $X^n(f)$ is the Fourier transform of $X(t)$, calculated in the time window $n\Delta t \leqslant t \leqslant n\Delta t + \Delta T$ of duration ΔT; Δt is the time interval between two successive windows. The averaging $\langle\ \rangle_n$ is performed on different sliding windows indexed by n. The cross-bicoherence level b_c varies between 0 and 1, equals 1 when the fields X, Y, and Z present perfect phase coherence at f_1, f_2, and $f_3 = f_1 + f_2$, respectively, and equals 0 in the absence of phase coherence.

Figure 2 shows the squared cross-bicoherence level, b_c^2, calculated for the field triad (B, E_z, B). The results are displayed in the (f_B, f_{E_z}) plane over a broad frequency range (panel (a)), as well as in focused views of the narrower frequency domains corresponding to the measured peaks (Figure 2(b)). The bicoherence reaches the high level $b_c \simeq 0.7$ at $(f_B, f_{E_z}) = (f_{\mathcal{Z}}, f_{\mathcal{S}}) \simeq (45.74, 0.3)$ kHz, which is a signature of the decay $\mathcal{LZ} \longrightarrow \mathcal{Z} + \mathcal{S}$, corresponding to the resonance condition $f_{\mathcal{LZ}} \simeq f_{\mathcal{Z}} + f_{\mathcal{S}}$, with $f_{\mathcal{LZ}} \simeq 46.04$ kHz. While the full frequency range includes small isolated regions with elevated cross-bicoherence levels (Figure 2(a)), these features correspond to waves with energies close to the noise floor (see Figure 1(f)), and should therefore be dismissed as nonphysical artifacts. In Figures 2(a) and (b), the triad (B, E_z, B) reveals elevated levels b_c exclusively in the region $(f_{\mathcal{Z}}, f_{\mathcal{S}})$. This precise localization shows a strong phase coherence only between the identified $\mathcal{S}$, $\mathcal{LZ}$, and $\mathcal{Z}$ waves. Moreover, the detected waves not only display such phase coherence but also satisfy resonance conditions and exhibit precise temporal synchronization—features that render spacecraft-related artifacts an improbable explanation for these observations.

To validate the robustness of our analysis, we computed the cross-bicoherence for all possible triads involving E_y or E_z in the second position (totaling 18 combinations) and averaged over the results (Figures 2(c), (d)). The cross-bicoherence level remains consistently high ($\langle b_c\rangle \simeq 0.7$), at the same frequencies as in panel (a), confirming that the nonlinear wave interaction identified in panels (a) and (b) persists upon averaging over all triads. Figure 2(c) shows lower cross-bicoherence peaks, which do not correspond to any physical signal, as evidenced in Figure 1(f). Since these spurious artifacts are absent for some triads (see panel (a)), their cross-bicoherence level is reduced through averaging. Finally, to demonstrate that the maximum cross-bicoherence b_c significantly exceeds the noise level, we used a surrogate data method with Fourier phase randomization (J. Theiler et al. 1992). With these surrogate data, the maximum cross-bicoherence falls to the noise floor,

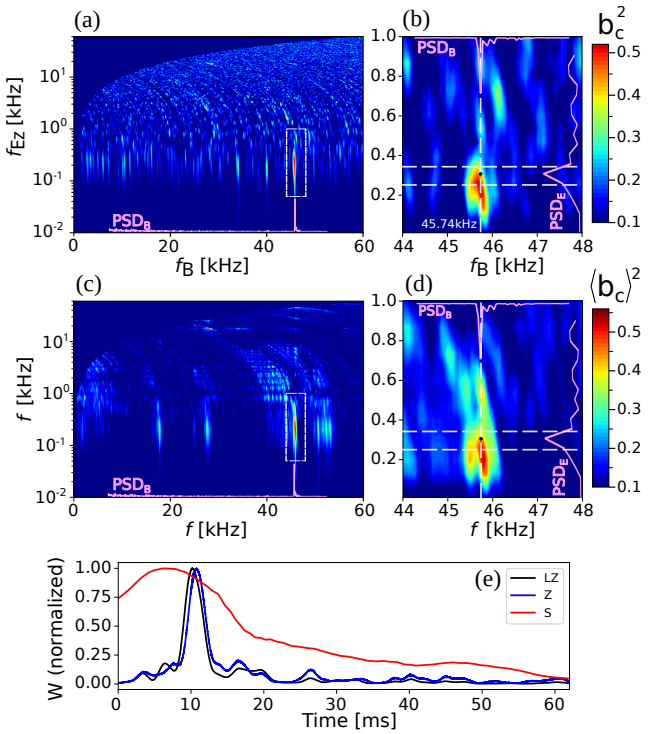

Figure 2. Determination of phase coherence between waves using cross-bicoherence. (a) Square of the cross-bicoherence, $b_c^2(f_B, f_{E_z})$, computed with the field triad (B, E_z, B) over the time interval of $0 \leqslant t \leqslant 62$ ms (see Equation (1) and the text), in the frequency ranges of $f_B, f_{E_z} \leqslant 60$ kHz. (b) Zoom-in of (a) in the map region with $44 \leqslant f_B \leqslant 48$ kHz and $f_{E_z} \leqslant 1$ kHz, where $b_c \simeq 0.7$ at $(f_B, f_{E_z}) = (f_{\mathcal{Z}}, f_{\mathcal{S}}) \simeq (45.74, 0.3)$ kHz (black dot). (c) Square of the cross-bicoherence averaged on 18 different triads with E_z or E_y in the second position, $\langle b_c\rangle^2$, in the same frequency range as (a). (d) Zoom-in of (c) in the same frequency range as in (b), with $\langle b_c\rangle \simeq 0.7$ at $(f_{\mathcal{Z}}, f_{\mathcal{S}})$ (black dot). (b), (d) The dashed white vertical lines indicate the local plasma frequency. The magenta curves represented on the upper and right borders of the panels reproduce the magnetic and low-frequency electric spectra (PSD$_B$ and PSD$_E$) used to calculate b_c, respectively (see Figures 1(h), (i)). (e) Variations with time of the $\mathcal{LZ}$, $\mathcal{Z}$, and $\mathcal{S}$ wave energies W (see the legend) obtained by integration of the wavelet spectrograms of the E, B, and E fields, respectively, in the range of $45.2 \leqslant f \leqslant 47.8$ kHz for the $\mathcal{LZ}$ and $\mathcal{Z}$-mode waves, and $f \leqslant 0.4$ kHz for the $\mathcal{S}$ waves.

estimated at approximately 0.3. The standard deviation of the surrogate cross-bicoherence distribution—representing the noise spread—is $\sigma_{b_c} \simeq 0.05$. Consequently, the measured peak with $b_c \simeq 0.7$ in Figures 2(c) and (d) deviates by $8\sigma_{b_c} \simeq 0.4$ above the noise floor, establishing its statistical significance. This result strongly suggests that the observed cross-bicoherence peaks reflect genuine phase coherence, not methodological artifacts. All subsequent bicoherence calculations were validated using this approach.

On the other hand, Figure 2(e) illustrates the time evolution of the energies carried by the $\mathcal{LZ}$, $\mathcal{S}$, and $\mathcal{Z}$-mode waves, derived by integrating the electric and magnetic energy spectrograms over their respective frequency bands (see the caption). A simultaneous increase in the energy of all three modes is observed, with a slight temporal offset of up to 2 ms. The close synchronization of the energy peaks highlights the strong temporal correlation between the three modes.

The presented arguments strongly support wave decay as the dominant mechanism that generates the observed $\mathcal{Z}$-mode waves. However, it may not act alone. Indeed, in plasmas with average levels $\Delta N = \langle(\delta n/n_0)^2\rangle^{1/2}$ of random density

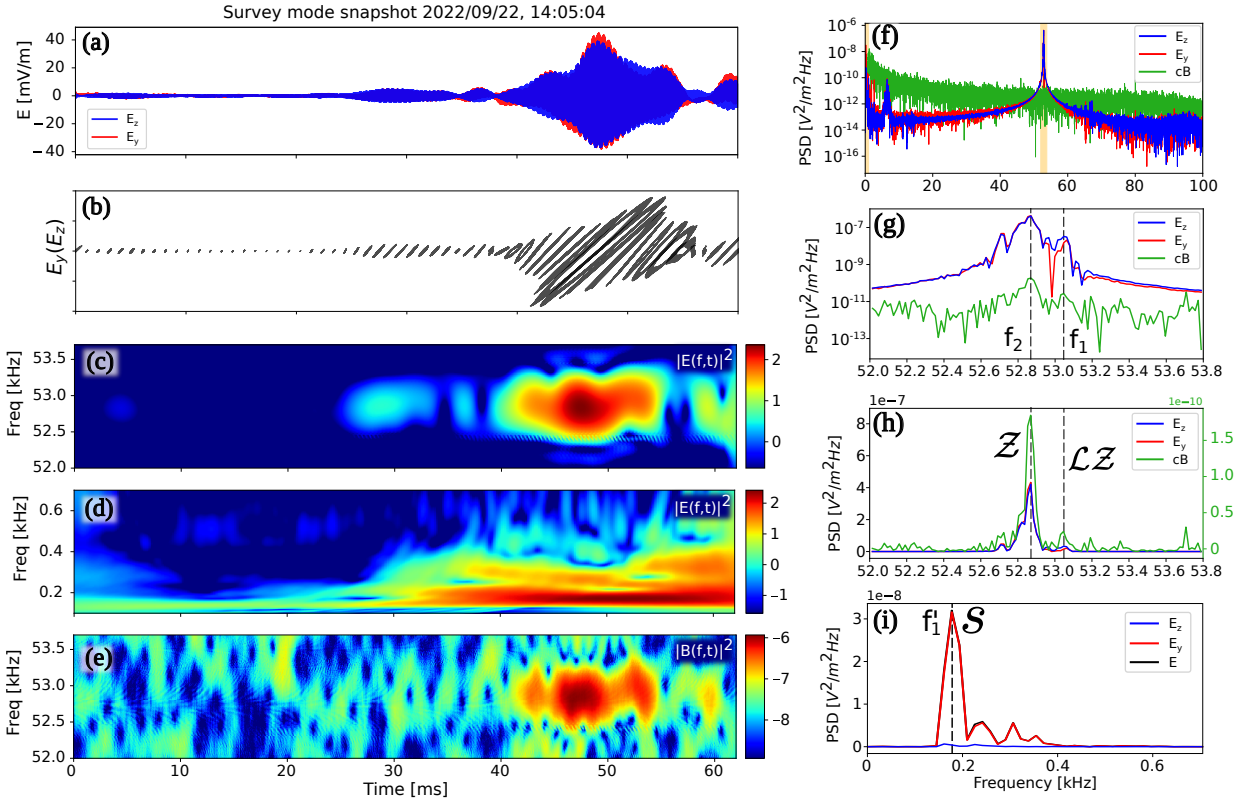

Figure 3. Snapshot captured by RPW on 2022 September 22, at 14:05:04 UT. (a) Waveform of the two electric field components E_z (blue) and E_y (red) in the SRF frame. (b) Hodograms $E_y(E_z)$ calculated within equidistant time windows of 0.7 ms. (c), (d) Wavelet spectrograms of the electric energy $|E(f,t)|^2$ in the high- and low-frequency ranges, i.e., $52 \leqslant f \leqslant 53.8$ kHz and $f \leqslant 0.7$ kHz, respectively. (e) Wavelet spectrogram of the magnetic energy $|B(f,t)|^2$, in the same frequency range as (c). (c)-(e) The color bars are in logarithmic scales. (f)–(i) Power spectra of E_z (blue), E_y (red), and cB (green), respectively. Zoomed-in views are presented, in linear scales, in the ranges of $52 \leqslant f \leqslant 53.8$ kHz (g), (h) and $f \leqslant 0.7$ kHz (i). (h), (i) Linear scales; the black curve represents the spectrum of $|E|^2$. The dashed vertical lines correspond to peaks at $f_2 \simeq 52.86$ kHz and $f_1 \simeq 53.05$ kHz (g), (h), and at $f_1' \simeq 0.18$ kHz (i). Spectra in (f)–(i) are calculated in the time interval of $0 \leqslant t \leqslant 62$ ms.

fluctuations of a few percent, the linear transformations of $\mathcal{LZ}$ waves on inhomogeneities can stimulate nonlinear wave–wave interactions (F. Polanco-Rodríguez et al. 2026). Moreover, plasma regions with gentle density fluctuations may also facilitate decay (C. Krafft & P. Savoini 2024a; C. Krafft et al. 2024b). By comparing observations with PIC simulations, we show that they are consistent with a scenario in which a $\mathcal{LZ}$ wave packet is trapped in a broad, nearly flat-bottomed density well, where a decay process can unfold (see Section 5 for more details).

4. Evidence of Decay to $\mathcal{Z}$-mode Waves during a Second Snapshot

In a snapshot recorded on 2022 September 22 at 14:0:04 UT —around 12 minutes after that presented in Section 3.1—clear signatures of $\mathcal{Z}$-mode waves generated through $\mathcal{LZ}$ wave decay are again detected. Figure 3 presents the corresponding waveforms and power spectra, presented in the same way as in Figure 1. At 14:05:04 UT, the beam is significantly relaxed (T. Formánek et al. 2025). Panel (a) highlights the emergence of a wave packet at $t \sim 50$ ms, with an amplitude reaching $\sim$40 mV m^{-1}, approximately one-fifth of the amplitude observed at 13:52:28 UT. This reduction is likely due to beam relaxation, which lowers the intensity of $\mathcal{LZ}$ wave turbulence. The waveform exhibits clear modulation of the field amplitude, suggesting the simultaneous presence of different high-frequency waves. The hodograms reveal a pattern similar to that observed at 13:52:28 UT, suggesting that the waves share the same polarization properties. At $t \simeq 45$ ms, the electric and magnetic energy spectrograms display pronounced peaks at frequency $f \sim 53$ kHz, consistent with $\mathcal{Z}$-mode wave radiation (Figures 3(c), (e)). Simultaneously, low-frequency emissions peak at $f \sim 0.2$ kHz (Figure 3(d)).

Figure 3(f) shows the electric and magnetic energy spectra over a broad frequency range. A zoomed-in view in panel (g) reveals three distinct high-frequency peaks at $f_1 \simeq 53.05$ kHz, $f_2 \simeq 52.86$ kHz, and $f_3 \simeq 52.71$ kHz. Meanwhile, the low-frequency spectrum shows a single peak at $f_1^{'} \simeq 0.18$ kHz (Figure 3(i)). The triad (f_2, f_1, f_1') satisfies the resonance condition $f_1 \simeq f_2 + f_1'$ with high precision, supporting the decay process $\mathcal{LZ} \longrightarrow \mathcal{Z} + \mathcal{S}$. In particular, the peak at $f_2 \simeq 52.86$ kHz reaches a pronounced maximum in the magnetic spectrum (Figure 3(h)), confirming its identification as a $\mathcal{Z}$-mode wave. The ratio $(E/cB)^2$ decreases from 10^4 at 53.05 kHz down to $5 \cdot 10^3$ at 52.86 kHz, which is consistent with the decay of mother $\mathcal{LZ}$ waves into electromagnetic $\mathcal{Z}$-mode waves near the boundary curve $k_*(\theta)$. However, the peak at $f_3 \simeq 52.71$ kHz does not satisfy any resonance relation with the low-frequency wave packet and is therefore unrelated to the wave–wave interactions. Similarly, as previously done, one easily checks that the threshold is exceeded and that $\varepsilon_0 E^2/4n_0 k_B T \simeq 2 \cdot 10^{-5}$ (with $k\lambda_D > 0.023$, as the beam velocity is lower than in the previous event), so that no strong turbulence process is expected (P. A. Robinson 1997). Note

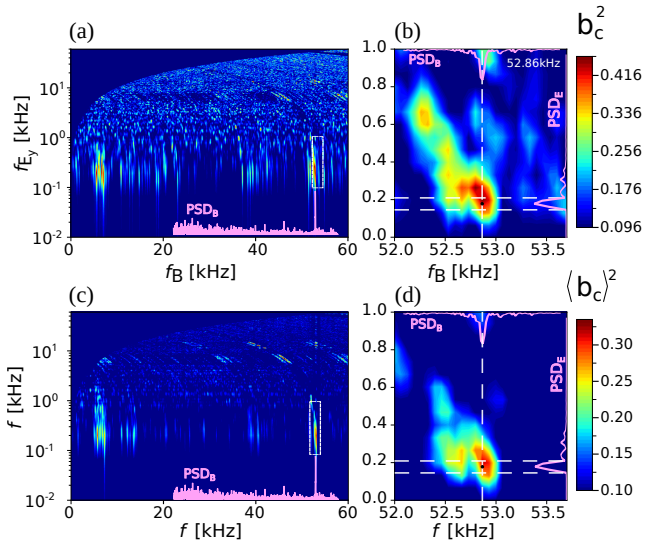

Figure 4. Determination of the phase coherence between waves using cross-bicoherence. (a) Square of the cross-bicoherence, $b_c^2(f_B, f_{E_y})$, calculated with the field triad (B, E_y, E_y) over the time interval of $0 \leqslant t \leqslant 62$ ms (see Equation (1) and the text), in the frequency range of $f_B, f_{E_y} \leqslant 60$ kHz. (b) Zoom-in of (a) in the domain $52 \leqslant f_B \leqslant 53.8$ kHz and $f_{E_y} \leqslant 1$ kHz, with $b_c \simeq 0.65$ at $(f_B, f_{E_y}) = (f_{\mathcal{Z}}, f_{\mathcal{S}}) \simeq (52.86, 0.18)$ kHz (black dot). (c) Square of the cross-bicoherence averaged over the 18 triads with E_y or E_z in the second position, $\langle b_c \rangle^2$, in the same frequency range as (a). (d) Zoom-in of (c), in the same frequency domain as (b), where $\langle b_c \rangle \simeq 0.55$ at $(f_{\mathcal{Z}}, f_{\mathcal{S}})$ (black dot). (b), (d) The dashed white vertical line indicates the local plasma frequency. The magenta curves represented on the upper and right borders of the panel reproduce the high- and the low-frequency spectra used to calculate b_c, respectively (see Figures 3(h), (i)).

that in Figures 3(g) and (h), the electric and magnetic spectra extend slightly down $f \simeq 52.80$ kHz, just below the dominant peak. This subtle feature could indicate the presence of weak scattering and LMC concurrently with the primary nonlinear process.

The nonlinear decay of $\mathcal{LZ}$ waves with $f_{\mathcal{LZ}} \simeq 53.05$ kHz is confirmed in Figure 4(b) by the high cross-bicoherence level $b_c \simeq 0.65$ found at $(f_{\mathcal{Z}}, f_{\mathcal{S}}) = (f_B, f_{E_y}) \simeq (52.86, 0.18)$ kHz. This corresponds precisely to the peaks of the high- and low-frequency spectra. Note that tests using surrogate data were performed (see Section 3.3). When averaged over the same 18 triads as described in Section 3.3, the cross-bicoherence decreases slightly to $\langle b_c \rangle \simeq 0.55$, while effectively suppressing noise and artifacts at other frequencies (panel (d)). Figures 4(a) and 4(c) show similar plots over the full frequency ranges; outside the regions highlighted in Figures 4(b) and 4(d), only low values of b_c can be observed. Note, however, a significant level of cross-bicoherence at $f \sim 8$ kHz, due to wave energy of an unidentified origin. However, as these waves are off-resonance with respect to the waves under study, they fall outside the scope of the present work.

5. Comparison with Numerical Simulations

Comparisons with 2D/3V PIC simulations can shed light on the above studies by offering a more complete view and a detailed understanding of the mechanisms at play. Figure 5(a) displays a waveform recorded by a virtual satellite moving in the simulation plane with velocity $|v_s| = 0.1 v_T$, in the direction antiparallel to the ambient magnetic field $\boldsymbol{B}_0$. This is consistent with the direction of the solar wind flow toward the outer solar system (in our case, the satellite is moving with respect to the plasma considered immobile). The simulations are performed using the Smilei code (J. Derouillat et al. 2018), and the main beam and plasma parameters match as close as possible the conditions expected near 0.5 au or measured by Solar Orbiter on 2022 September 22, i.e., $f_c/f_p = 0.02$, $v_b = 0.25c$, and $\Delta N = \langle (\delta n/n_0)^2 \rangle^{1/2} = 0.025$. The analysis is now enriched by new parameters, including the local plasma frequency, the six field components, the ion and electron densities, as well as the full set of beam-plasma conditions. Dimensionless variables are used below. In particular, time and frequencies are normalized by f_p, the ion density n_i by the average plasma density n_0. Fields and energies are presented in arbitrary units. As the beam velocity, the ambient magnetic field is directed along the x-axis; the simulation plane is (x, y) (see C. Krafft & P. Savoini 2021, 2022 and C. Krafft et al. 2024b, 2025 for more technical details).

The electric field waveform features a distinct wave packet centered at $t \simeq 1500 f_p^{-1}$, which exhibits significant amplitudes in both the parallel and perpendicular components $E_\parallel = E_x$ and $E_\perp \simeq E_y$ with respect to $\boldsymbol{B}_0$ (Figure 5(a)). This isolated packet is observed as the virtual satellite crosses a shallow density depletion, where the normalized ion density reaches $n_i/n_0 \simeq 0.985$ over the time interval of $[500, 4500] f_p^{-1}$. The electric energy spectrogram shows that the wave packet is composed of $\mathcal{LZ}$ waves with frequencies distributed around the local plasma frequency f_{pl} (white line in Figure 5(b)), due to weak wave scattering on density fluctuations δn. Later, at $f_p t \gtrsim 2000$, large-k (Doppler-shifted) $\mathcal{LZ}$ waves appear slightly above f_{pl}, characterized by minimal magnetic signatures.

The low-frequency energy spectrogram $|\delta n_i(f, t)/n_0|^2$ (Figure 5(c)), where $\delta n_i = n_i - n_0$, reveals pronounced ion acoustic wave emissions (C. Krafft & P. Savoini 2024a) with frequencies around $0.01 f_p$. Meanwhile, Figure 5(d), which presents the magnetic energy spectrogram $|B_{\mathcal{LZ}}(f, t)|^2 \simeq |B_x(f, t)|^2 + |B_y(f, t)|^2$ carried by the $\mathcal{LZ}$ waves (F. Polanco-Rodríguez et al. 2025b), displays large-amplitude emissions around f_p. Those temporally coincide with the intense low- and high-frequency electric wave activity. At this point, a striking similarity emerges between the waveforms and spectrograms of Figures 1 and 5, which supports our interpretation of both Solar Orbiter observations.

Figures 5(e)–(g) present the high-frequency electric and magnetic spectra, along with the low-frequency one, which is obtained here from the ion density perturbations $\delta n_i = n_i - n_0$ directly, and not from the low-frequency electric fields, as in the above sections. Figure 5(e) highlights four $\mathcal{LZ}$ wave energy peaks, at $f_4 \simeq 0.992 f_p$, $f_3 \simeq 0.999 f_p$, $f_2 \simeq 1.004 f_p$, and $f_1 \simeq 1.012 f_p$. This spectral complexity reflects the underlying wave turbulence trapped within the density well ($500 \lesssim f_p t \lesssim 4500$). In this gently inhomogeneous region, several wave packets coexist simultaneously, though not all participate in the nonlinear decay. Furthermore, they correspond to significant magnetic signatures with $(E/cB)^2 \sim 10^4$ (Figure 5(f)), except at f_4 and f_1, where $(E/cB)^2 \simeq 2 \cdot 10^5$ and $(E/cB)^2 \simeq 3 \cdot 10^6$, respectively. The peak observed at $f_3 = f_{\mathcal{Z}} \simeq 0.999 f_p$ is attributed to $\mathcal{Z}$-mode waves generated through the nonlinear decay of $\mathcal{LZ}$ waves, as discussed below. In contrast, the peak at $f_4 \simeq 0.992 f_p$ corresponds to $\mathcal{LZ}$ waves, likely resulting from scattering on density fluctuations,

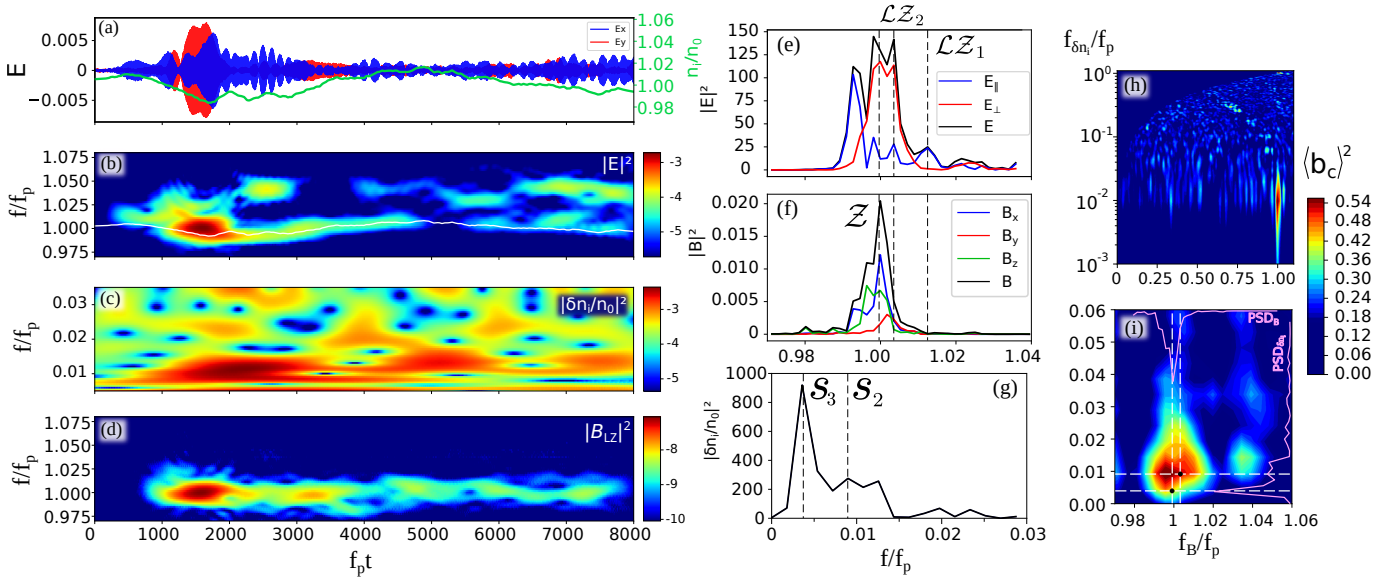

Figure 5. Waveform recorded by a virtual satellite moving into a 2D PIC simulation plane with the velocity $|v_s| = 0.1v_T$, in the direction opposite to $\mathbf{B}_0$. Plasma and beam parameters are $\Delta N = 0.025$, $f_c/f_p = 0.02$, and $v_b = 0.25c$. (a) Waveforms of the parallel $E_\parallel = E_x$ (blue) and perpendicular $E_\perp \simeq E_y$ (red) electric fields (E_z is negligibly small). The green line represents the normalized ion density n_i/n_0 (right axis). (b) Spectrograms of the electric energy $|E(f, t)|^2 = |E_x(f, t)|^2 + |E_y(f, t)|^2 + |E_z(f, t)|^2$ in the frequency range of $0.97 \leqslant f/f_p \leqslant 1.08$; the white line represents the local plasma frequency f_{pl} normalized to the average plasma frequency f_p. (c) Spectrogram of $|\delta n_i(f, t)/n_0|^2$ in the range of $0.005 \leqslant f/f_p \leqslant 0.035$. (d) Spectrogram of $|\boldsymbol{B}_{\mathcal{LZ}}(\boldsymbol{f}, \boldsymbol{t})|^2$in the same frequency range as (b). (e) Power spectra of the electric field energy $|E(f)|^2$ (black), in the range of $0.97 \leqslant f/f_p \leqslant 1.04$; the parallel and perpendicular energies are shown in blue and red, respectively. (f) Power spectra of the magnetic field energy $|B(f)|^2$ (black), in the same frequency range as (e); the three field components are indicated in color. (e), (f) Spectra are calculated in the time interval of $500 \leqslant f_p t \leqslant 4000$. (g) Low-frequency power spectrum $|\delta n_i(f)/n_0|^2$ in the range of $f/f_p \leqslant 0.03$. (e), (g) Vertical dashed lines indicate the frequencies $f_3 \simeq 0.999f_p$, $f_2 \simeq 1.004f_p$ and $f_1 \simeq 1.012f_p$ (e), (f) as well as $f_3' \simeq 0.004f_p$ and $f_2' \simeq 0.009f_p$ (g). (h), (i) Square of the cross-bicoherence averaged on the 4 triads (B_x, δn_i, E_x), (B_y, δn_i, E_x), (B_x, δn_i, E_y), and (B_y, δn_i, E_y), in the ranges of $f_B/f_p \leqslant 1.1$ and $f_{\delta n_i}/f_p \leqslant 1$ (h), as well as $0.97 \leqslant f_B/f_p \leqslant 1.06$ and $f_{\delta n_i}/f_p \leqslant 0.06$ (i). Black dots indicate the position of the average cross-bicoherence $\langle b_c \rangle \simeq 0.73$ and $\langle b_c \rangle \simeq 0.65$ obtained for the decay processes $\mathcal{LZ}_1 \longrightarrow \mathcal{LZ}_2 + \mathcal{S}_2$ and $\mathcal{LZ}_2 \longrightarrow \mathcal{Z} + \mathcal{S}_3$, respectively.

Doppler-shift effects, or a combination of both. Since the peak is off-resonance with other waves, it is not analyzed further. Finally, the spectrum $|\delta n_i(f)/n_0|^2$ of the ion density perturbations reveals ion acoustic waves with energy maxima at $f_3' = 0.004f_p$, $f_2' = 0.009f_p$, and $f_1' = 0.0125f_p$ (Figure 5(g)).

Two three-wave frequency resonance conditions can be identified: $f_{\mathcal{LZ}_1} \simeq 1.012f_p \simeq f_{\mathcal{LZ}_2} + f_{\mathcal{S}_2} \simeq 1.004f_p + 0.009f_p$ and $f_{\mathcal{LZ}_2} \simeq 1.004f_p \simeq f_{\mathcal{Z}} + f_{\mathcal{S}_3} \simeq 0.999f_p + 0.004f_p$. First, the waves $\mathcal{LZ}_1$ decay into daughter waves through the channel $\mathcal{LZ}_1 \longrightarrow \mathcal{LZ}_2 + \mathcal{S}_2$, which is followed by a subsequent decay cascade, $\mathcal{LZ}_2 \longrightarrow \mathcal{Z} + \mathcal{S}_3$, which deposits high-frequency wave energy at $f_{\mathcal{Z}} \simeq 0.999f_p$. It should be noted that the $\mathcal{LZ}_1$ waves are not driven directly by the beam. Instead, they likely arise from another wave process. Their relatively small wavevectors enable them to decay into $\mathcal{Z}$-mode waves through two successive decay cascades only. The significantly lower energy carried by $\mathcal{LZ}_1$ waves compared to $\mathcal{LZ}_2$ waves can be attributed to the reasons discussed in Section 3.2.1.

The decay processes are corroborated by cross-bicoherence diagnostics, as illustrated in Figures 5(h) and (i), which reveal strong phase coherence within both the wave triads ($\mathcal{LZ}_1$, $\mathcal{LZ}_2$, $\mathcal{S}_2$) and ($\mathcal{LZ}_2$, $\mathcal{Z}$, $\mathcal{S}_3$), respectively. The cross-bicoherence levels, obtained by averaging over four different triads (see the caption), reach $\langle b_c \rangle \simeq 0.65$ at $(f_{\mathcal{Z}}, f_{\mathcal{S}_3}) = (0.999, 0.004)f_p$, and $\langle b_c \rangle \simeq 0.73$ at $(f_{\mathcal{LZ}_2}, f_{\mathcal{S}_2}) = (1.004, 0.009)f_p$, respectively (see the black dots in panel (i)). Additionally, Figure 5(h) shows that the significant cross-bicoherence levels are strictly confined within a small frequency region. Tests using surrogate data were performed (see Section 3.3).

In addition to the features observed in the simulations that closely mirror those captured in the Solar Orbiter snapshots, some suggestions can be inferred. First, the isolated location of the large-amplitude wave packets, as shown in Figures 1 and 3, can be attributed to wave trapping within a density well. In nearly homogeneous plasmas with minimal density turbulence, $\mathcal{LZ}$ wave energy does not exhibit such localization effects (F. Polanco-Rodríguez et al. 2025a, 2026). Second, the frequencies of the intense $\mathcal{LZ}$ waves in Figures 1(c) and 5(b) exhibit slight and smooth temporal variations. In Figure 5(b), they follow the local plasma frequency. When applied to Solar Orbiter observations, this suggests that the wave packets are likely confined within a density depletion. In such a case, the decay process would remain dominant over scattering and mode conversion, indicating that the density well should be both extended and characterized by a nearly flat bottom.

6. Conclusion

During a type III radio burst, the Solar Orbiter spacecraft encountered an electron beam and captured high-resolution electric and magnetic waveforms. Based on these observations, this study presents the first evidence in the solar wind of the nonlinear decay of beam-driven $\mathcal{LZ}$ waves into electromagnetic $\mathcal{Z}$-mode radiation near f_p. The three-wave interaction process is evidenced through several key findings: (i) the Doppler-shifted frequency resonance conditions are satisfied, involving frequencies and wavevectors in the solar wind frame, (ii) strong phase coherence exists between the waves, (iii) the interacting modes coincide temporally, and (iv) the results align closely with theoretical predictions, including the decay threshold, the turbulence parameter of $\mathcal{LZ}$ waves, and the two-dimensional decay kinematics and dynamics. In

addition, a second waveform revealing the same decay process is presented. PIC simulations, conducted under close beam-plasma conditions, successfully replicate the observations, reinforcing the results. Notably, they suggest that the wave packets observed by Solar Orbiter may be trapped within an extended, nearly flat-bottomed density well, where the decay process is not overcome by wave scattering on random density fluctuations and subsequent mode conversion effects.

These results stem from recent key developments: first, the progress in in situ magnetometry, which allowed for the unambiguous identification of $\mathcal{Z}$-mode waves; second, the foundational theoretical work—validated through PIC simulations—that enabled the identification of the process driving their generation; and third, the methodology that connects in situ spacecraft measurements and large-scale, long-term 2D/3V PIC simulations through the virtual satellite technique. Modern missions such as Parker Solar Probe and Solar Orbiter offer an ideal platform for applying and further developing this approach.

Acknowledgments

This work was granted access to the HPC computing and storage resources under the allocation 2023-A0130510106 and 2024-A017051010 made by GENCI. This research was also financed in part by the French National Research Agency (ANR) under the project ANR-23-CE30-0049-01. C.K. thanks the International Space Science Institute (ISSI) in Bern through ISSI International Team project No. 557, Beam-Plasma Interaction in the Solar Wind and the Generation of type III Radio Bursts. C. K. thanks the Institut Universitaire de France (IUF). The authors thank T. Chust, T. Dudok de Wit, D. Fontaine, and M. Kretzschmar for offering their expertise in satellite data analysis.

Solar Orbiter is a mission of international cooperation between ESA and NASA, operated by ESA. The RPW instrument has been designed and funded by CNES, CNRS, the Paris Observatory, the Swedish National Space Agency, ESA-PRODEX, and all the participating institutes.

For open access purposes, a CC-BY license has been applied by the authors to this document and will be applied to any subsequent version up to the author's manuscript accepted for publication resulting from this submission.

ORCID iDs

F. J. Polanco-Rodríguez https://orcid.org/0009-0005-2951-697X
C. Krafft https://orcid.org/0000-0002-8595-4772
P. Savoini https://orcid.org/0000-0002-2117-3803

References

Akimoto, K. 1989, PhFlB, 1, 1998
Bale, S. D., Kellogg, P. J., Goetz, K., & Monson, S. J. 1998, GeoRL, 25, 9
Bale, S. D., Larson, D. E., Lin, R. P., et al. 2000, JGR, 105, 27353
Bale, S. D., Goetz, K., Harvey, P. R., et al. 2016, SSRv, 204, 49
Cairns, I. H., & Layden, A. 2018, PhPl, 25, 082309
Derouillat, J., Beck, A., Pérez, F., et al. 2018, CoPhC, 222, 351
Formánek, T., Santolík, O., Souček, J., et al. 2025, ApJL, 985, L29
Fox, N. J., Velli, M. C., Bale, S. D., et al. 2016, SSRv, 204, 7
Gary, S. P. 1993, Theory of Space Plasma Microinstabilities (Cambridge Univ. Press)
Graham, D. B., & Cairns, I. H. 2013, JGR, 118, 3968
Henri, P., Briand, C., Mangeney, A., et al. 2009, JGR, 114, A03103
Jannet, G., Dudok de Wit, T., Krasnoselskikh, V., et al. 2021, JGR, 126, e28543
Jebaraj, I. C., Krasnoselskikh, V., Pulupa, M., Magdalenic, J., & Bale, S. D. 2023, ApJL, 955, L20
Kellogg, P. J., Goetz, K., Monson, S. J., & Opitz, A. 2013, JGR, 118, 4766
Krafft, C., & Savoini, P. 2021, ApJL, 917, L23
Krafft, C., & Savoini, P. 2022, ApJL, 924, L24
Krafft, C., & Savoini, P. 2023, ApJ, 949, 24
Krafft, C., & Savoini, P. 2024a, ApJL, 964, L30
Krafft, C., Savoini, P., & Polanco-Rodríguez, F. J. 2024b, ApJL, 967, L20
Krafft, C., & Volokitin, A. S. 2025, ApJS, 281, 67
Krafft, C., Volokitin, A. S., & Krasnoselskikh, V. V. 2013, ApJ, 778, 111
Krafft, C., Volokitin, A. S., Polanco-Rodríguez, F. J., & Savoini, P. 2025, NatAs, 9, 1292
Krauss-Varban, D. 1989, JGR, 94, 3527
Kretzschmar, M., Vecchio, A., Krasnoselskikh, V., et al. 2026, ApJL, 1001, L24
Larosa, A., de Wit, T. D., Krasnoselskikh, V., et al. 2022, ApJ, 927, 95
Layden, A., Cairns, I. H., Li, B., & Robinson, P. A. 2013, PhRvL, 110, 185001
Lin, R. P., Levedahl, W. K., Lotko, W., Gurnett, D. A., & Scarf, F. L. 1986, ApJ, 308, 954
Ma, B., Chen, L., Wu, D., Ning, Z., Bale, S. D., et al. 2026, ApJ, 998, 316
Maksimovic, M., Bale, S. D., Chust, T., et al. 2020, A&A, 642, A12
Malaspina, D. M., Cairns, I. H., & Ergun, R. E. 2011, GeoRL, 38, L13101
Müller, D., St. Cyr, O. C., Zouganelis, I., et al. 2020, A&A, 642, A1
Polanco-Rodríguez, F., Krafft, C., & Savoini, P. 2025a, ApJL, 989, L38
Polanco-Rodríguez, F., Krafft, C., & Savoini, P. 2025b, ApJL, 982, L24
Polanco-Rodríguez, F., Krafft, C., & Savoini, P. 2026, arXiv:2601.09368
Robinson, P. A. 1997, RvMP, 69, 507
Sagdeev, R. Z., & Galeev, A. A. 1969, Nonlinear Plasma Theory (Benjamin)
Shukla, P. K., Yu, M. Y., Mohan, M., Varma, R. K., & Spatschek, K. H. 1983, PhRvA, 27, 552
Soucek, J., Píša, D., Kolmasova, I., et al. 2021, A&A, 656, A26
Theiler, J., Eubank, S., Longtin, A., Galdrikian, B., & Doyne Farmer, J. 1992, PhyD, 58, 77
Zakharov, V. E., Musher, S. L., & Rubenchik, A. M. 1985, PhR, 129, 285